Energy & Environmental Science

ROYAL SOCIETY OF CHEMISTRY

PAPER

View Article Online
View Journal | View Issue

Cite this: *Energy Environ. Sci.*, 2024, **17**, 2007

A nature-inspired solution for water management in flow fields for electrochemical devices†

Panagiotis Trogadas, ‡[a] Jason I. S. Cho,‡*[a] Lara Rasha, [b] Xuekun Lu, [b] Nikolay Kardjilov, [c] Henning Markötter,[c] Ingo Manke, [c] Paul R. Shearing, [b] Dan J. L. Brett [b] and Marc-Olivier Coppens *[a]

Received 27th October 2023,
Accepted 6th February 2024

DOI: 10.1039/d3ee03666a

rsc.li/ees

A systematic, nature-inspired chemical engineering approach is employed to solve the issue of flooding in electrochemical devices. The mechanism of passive water transport utilized by lizards living in arid environments is leveraged to design flow-fields with a microchannel structure on their surface, through which capillary pressure rapidly removes the water generated in the electrochemical device. This water management strategy is implemented in proton exchange membrane fuel cells (PEMFCs) with a lung-inspired flow-field, which ensures uniform distribution of reactants across the catalyst layer. Jointly, this nature-inspired approach results in flood-free, stable operation at 100% RH and a ~60% increase in current (~1.9 A cm^{-2}) and peak power density (~650 mW cm^{-2}) compared to current PEMFCs with a flood-prone, serpentine flow-field (~0.8 A cm^{-2} and 280 mW cm^{-2}, respectively). This significant advance allows for PEMFC operation at fully humidified conditions.

Broader context

Water management within electrochemical devices is pivotal, as flooding is detrimental to their longevity and performance. Proposed solutions are dominated by empiricism and there are significant gaps between computational design, materials synthesis, and electrochemical device prototyping, which leads to flood-prone fuel cells with sub-optimal performance. This article details a new direction to engineer flow fields for proton exchange membrane fuel cells (PEMFCs) that, exceptionally, do not flood even at relative humidity close to 100% RH, and continue to achieve high performance. To streamline and accelerate the design process, a systematic and holistic nature-inspired chemical engineering (NICE) approach is employed. NICE leverages universal mechanisms in nature underpinning desired properties (such as efficiency, scalability, and resilience) and incorporates them effectively into engineering design. Unlike typical biomimetic approaches, NICE does not copy nature, but is rooted in fundamentals, and makes adaptations that account for the differences in context between nature and technical applications. Beyond scalable water management in PEMFCs, the systematic NICE methodology can and has been used to accelerate innovation in a wide range of applications, from water purification and sustainable manufacturing to healthcare.

Introduction

Hydrogen is increasing in importance as an energy vector, specifically green hydrogen, which is expected to be one of the protagonists (up to ~24% share in the energy mix by 2050)[1] in global decarbonization efforts.[2,3] Reducing greenhouse gas emissions from the long-distance, difficult-to-decarbonize transportation sector is of vital importance since its emissions represent ~25% of global CO_2 emissions.[4] In the case of light-duty transportation, battery powered electric vehicles (BEVs) are rapidly infiltrating the market with ~14% share in global car sales in 2022[5] despite their relatively long charging times and limited range (~100–350 miles compared to 450 miles from a tank of gasoline).[6] Fuel cell powered electric vehicles (FCVs) can complement BEVs offering long driving range similar to internal combustion engine vehicles and rapid refueling.[7,8] However, their market growth is slow and below expectations[9] due to technological challenges (such as the long-term durability of proton exchange membrane fuel cell (PEMFC) stacks, flooding at high relative humidity (RH), mass-production of high-pressure hydrogen tanks), the high cost of FCVs, and the limited number of automakers mass producing such vehicles.[9] On the contrary, PEMFC technology is expected to dominate freight

[a] *EPSRC "Frontier Engineering" Centre for Nature Inspired Engineering, Department of Chemical Engineering, University College London, London, WC1E 7JE, UK. E-mail: in.cho.13@alumni.ucl.ac.uk, m.coppens@ucl.ac.uk*
[b] *Electrochemical Innovation Lab, Department of Chemical Engineering, University College London, London, WC1E 7JE, UK*
[c] *Helmholtz-Zentrum Berlin, Hahn-Meiitner-Platz 1, 14109, Berlin, Germany*

† Electronic supplementary information (ESI) available. See DOI: https://doi.org/10.1039/d3ee03666a

‡ Both authors contributed equally.

transportation (ships, trains, heavy lorries) soon, since its power output can be easily scaled up *via* an increase of the size of the stack or the hydrogen tank at a lower additional weight cost than a lithium-ion battery,[10] with PEMFC powered prototypes gradually infiltrating the market.[4,10–12]

However, the current PEMFC technology is not mature enough to meet the 80 000 h and 8000 h durability targets (2020–2025) for stationary and transportation applications, respectively.[13] This lack of durability is associated with the degradation of the key component of PEMFC, namely the membrane electrode assembly (MEA), and is related to the operating conditions: load cycling between open-circuit potential of 1 V *vs.* reversible hydrogen electrode (RHE) and optimum operating point (0.5–0.7 V *vs.* RHE), and 20–60% relative humidity (RH).[14,15] Operation with fully humidified gas (100% RH) is rare, except during transient conditions such as start-up, shutdown, and high power loading.[16] The MEA consists of a proton exchange membrane sandwiched between catalyst layers and gas diffusion layers. The catalyst layer (Pt/C) on each side of the membrane enables hydrogen oxidation (anode) and oxygen reduction (cathode) reactions, while the membrane allows protons to pass through from the anode to the cathode, keeping the gases separate. The degradation of the catalyst (platinum dissolution and sintering), support (carbon corrosion), and polymer membrane are key factors that can reduce the lifespan of a PEMFC.[14,15]

Flooding is detrimental to the longevity and performance of a PEMFC since it reduces the electrochemically active surface area and hinders gas transport to or from the reaction sites.[17,18] A voltage decay rate of $\sim$0.5 mV h^{-1} as well as a $\sim$55% decrease in current density ($\sim$0.6 A cm^{-2} to $\sim$0.3 A cm^{-2}), 66% decrease in peak power density ($\sim$700 mW cm^{-2} to $\sim$250 mW cm^{-2}), and 34% decrease in electrochemically active surface area (ECSA) ($\sim$59 m^2 g^{-1} to $\sim$39 m^2 g^{-1}) are reported after only 600 h operation at fully humidified conditions (25 cm^2 PEMFC, H_2/air as fuel/oxidant).[19] A similar voltage decay rate ($\sim$0.8 mV h^{-1}) is observed in the case of a 5 cm^2 PEMFC operating at 100% RH for 200 h (H_2/air as fuel/oxidant), demonstrating a $\sim$20% decrease in current ($\sim$0.8 A cm^{-2} to 0.65 A cm^{-2}) and 40% (283 mW cm^{-2} to 171 mW cm^{-2}) decrease in peak power density.[20]

To alleviate this issue, several approaches have been used including the engineering of new flow-fields (radial, wave form, parallel serpentine-baffle),[21] and the incorporation of a microporous layer ($\sim$0.5–15 μm pore size) in between the gas diffusion electrode and the catalyst layer.[22] Alteration of the shape of the flow-field negatively affects the performance of the PEMFC due to the low pressure drop and flow velocity in these flow-fields, causing the produced water to accumulate at the outlet of the flow channel,[21] while, even though the incorporation of a microporous layer improves water management in the PEMFC, its synthesis procedure is tedious and requires several steps increasing the cost of the final product.[22]

Water management is also essential in alkaline, high-temperature proton exchange membrane and unitized regenerative fuel cells, as well as CO_2 electrolyzers. The flooding of alkaline fuel cells is more severe than in PEMFCs as the distribution of water within the cell is non-uniform resulting in a flood-prone anode and a dried-out cathode, and hence to non-reversible potential losses, instability, and chemical degradation of the electrocatalyst.[23,24] Flow-fields must be designed to achieve a delicate balance between the humidity conditions of the reactants in the anode and cathode, minimizing the possibility of under-hydration (*i.e.* cathode dry-out) and over-hydration (*i.e.* flooding of the anode and cathode).[23,24] The flooding of the cathode is also detrimental to the performance of unitized regenerative fuel cells, significantly reducing the available active sites of the catalyst and hence increasing the potential losses in the cathode at high current density.[25] CO_2 electrolyzers (microfluidic and zero-gap reactors) face the same issue leading to cathode starvation of CO_2 and promotion of the competing hydrogen evolution reaction. As a result, there is a significant decrease in product selectivity and efficiency of the device.[26,27] Even though water flooding is not as severe in high-temperature fuel cells, because the high operating temperature can evaporate the water rapidly, an effective water management strategy is still required to alleviate dehydration of the anode, leading to the degradation of electrocatalyst and polymer membrane.[28]

Rather than recycling the same approaches, we employ nature-inspired chemical engineering (NICE)[29,30] to tackle the flooding issue. Recently, we applied this systematic nature-inspired solution methodology[30,31] to address the issue of non-uniform distribution of reactants across the catalyst layer of a PEMFC. Rather than imitating nature out of context, as in narrow biomimicry, the NICE approach is based on fundamental understanding of key principles underpinning desirable, superior features in biological and other natural systems, such as scalability, robustness, and efficiency. This conceptual insight is incorporated into the design of a target application, such as flow-field design of PEMFCs, which uses these key, natural principles to enable transformative improvements. This is achieved while considering the different context and constraints between the fuel cell technology and the chosen biological model.

An example of a natural system that has a similar role to PEMFC flow-fields, and is used as a guide for their design, is the human lung. Its primary purpose is the uniform distribution of air throughout its volume and the oxygenation of the bloodstream.[31,32] Its fractal structure ensures scale-independent, uniform gas distribution throughout the pulmonary volume, from trachea to alveoli, while also achieving minimal global entropy production. The structure changes from a branched, self-similar tree that obeys Murray's law in the upper airway tree (bronchi) to a more uniform architecture in the lower part (acini), commensurate with a transition from convective to diffusive transport (Péclet number, Pé $\sim$ 1).[31–34] Numerical simulations of lung-inspired flow-field based PEMFCs, with 10 cm^2 surface area, demonstrate that the ideal number of generations (N) for minimal entropy production lies between 4 and 7. Based on these simulation results, three flow-fields with N = 3, 4, and 5 generations were 3D printed and compared to commercial serpentine flow-field based PEMFCs.[31,32] The lung-inspired flow-field based PEMFC with N = 4 generations demonstrated a $\sim$20% and $\sim$30% increase in current and power density, respectively, over serpentine

flow-field based PEMFCs above 0.8 A cm^{-2}.[31] However, the performance of both lung-inspired and serpentine flow-field based PEMFCs deteriorates due to flooding at 100% relative humidity (RH), with lung-inspired flow-field based PEMFC demonstrating ~10% lower performance than serpentine flow-field based PEMFC.[31] The flooding of channels in fractal flow-fields is not desirable, as the gas is redistributed within the fractal distributor network, and leads to an exponential decay of the cell potential.[35]

Inspiration from nature: passive water movement

To address this severe flooding issue of PEMFCs at high RH, is there an example in nature that can serve as a source of inspiration? Here, it is informative to learn from animals living in arid environments and the mechanisms they employ to ingest scarce water from damp sand or dew. Examples include several lizards residing in the desert, such as the Australian thorny devil (*Moloch horridus*, *Agamidae*) and Texan horned lizard (*Phrynosoma cornutum*, *Iguanidae*), which possess the remarkable "water harvesting" ability to collect water with their integument.[36–41] Due to their anatomy, these lizards cannot ingest water by conventional means (*i.e.*, licking), since their mouth is specifically designed to eat ants.[37–40] Rather, they have to rely on the passive transport of water across the outer layer of their integument *via* capillary action.[36–40] This mechanism of passive water transport is based on the hydrophilicity of their integument and geometric principles: the intricate network of interconnected capillary channels (with ~100–150 μm diameter and ~50–200 μm depth[42]) between the overlapping scales[37,38,42,43] on the outer layer of their integument generates capillary pressure, which enables the passive water transport across their integument. Once the capillary channels are saturated, water transport through capillaries ceases and water has to be ingested at the jaw to keep the water flow uninterrupted in the integumental capillary channels towards the snout.[44]

Engineering of lung-inspired flow-fields with integrated capillary array

The unique mechanism employed by these lizards to ingest water inspires a solution to the flooding issue in PEMFCs at high RH (Fig. 1). Based on the geometric principles of the water harvesting channels on the integument of these lizards, we engineered a thin graphite plate of 1.2 mm with laser-engraved capillaries on its surface (Fig. 2(b) and Section S1.4, ESI†). We used the maximum power setting of a compact laser micromachining system (Section S1.2, ESI†) to create 252 interconnected capillaries with suitable dimensions that would reproduce the water harvesting realised through the integument of the lizards (Fig. 2(b)–(d)).

To verify that the unique characteristic of the water drinking mechanism utilized by lizards (water transport *via* capillary forces) is preserved despite the scale-up of the natural model

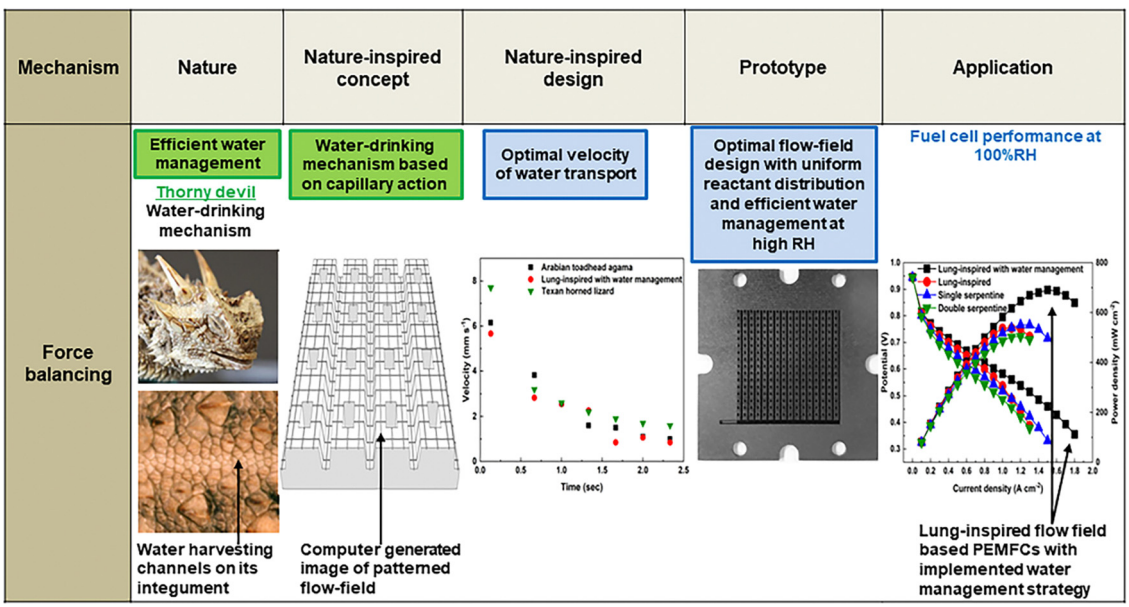

Fig. 1 Systematic, step-by-step application of the NICE approach for the design and engineering of a lung-inspired flow-field (N = 4 generations, 10 cm^2 surface area) based PEMFC with an integrated capillary array (LUCY). Inspiration is derived from the water-drinking mechanism employed by lizards residing in arid environments. This mechanism is based on the passive transport of water across their hydrophilic integument by an interscalar saw-tooth-shaped capillary network towards their snout. A compact laser micromachining system is used for the engineering of LUCY, which is then installed in a PEMFC. The water management and performance of LUCY flow-field based PEMFCs are evaluated *via* neutron radiography and polarization measurements at fully humidified conditions, respectively. The images of thorny devil and its integument are reproduced with permission from ref. 38 (Creative Commons License).

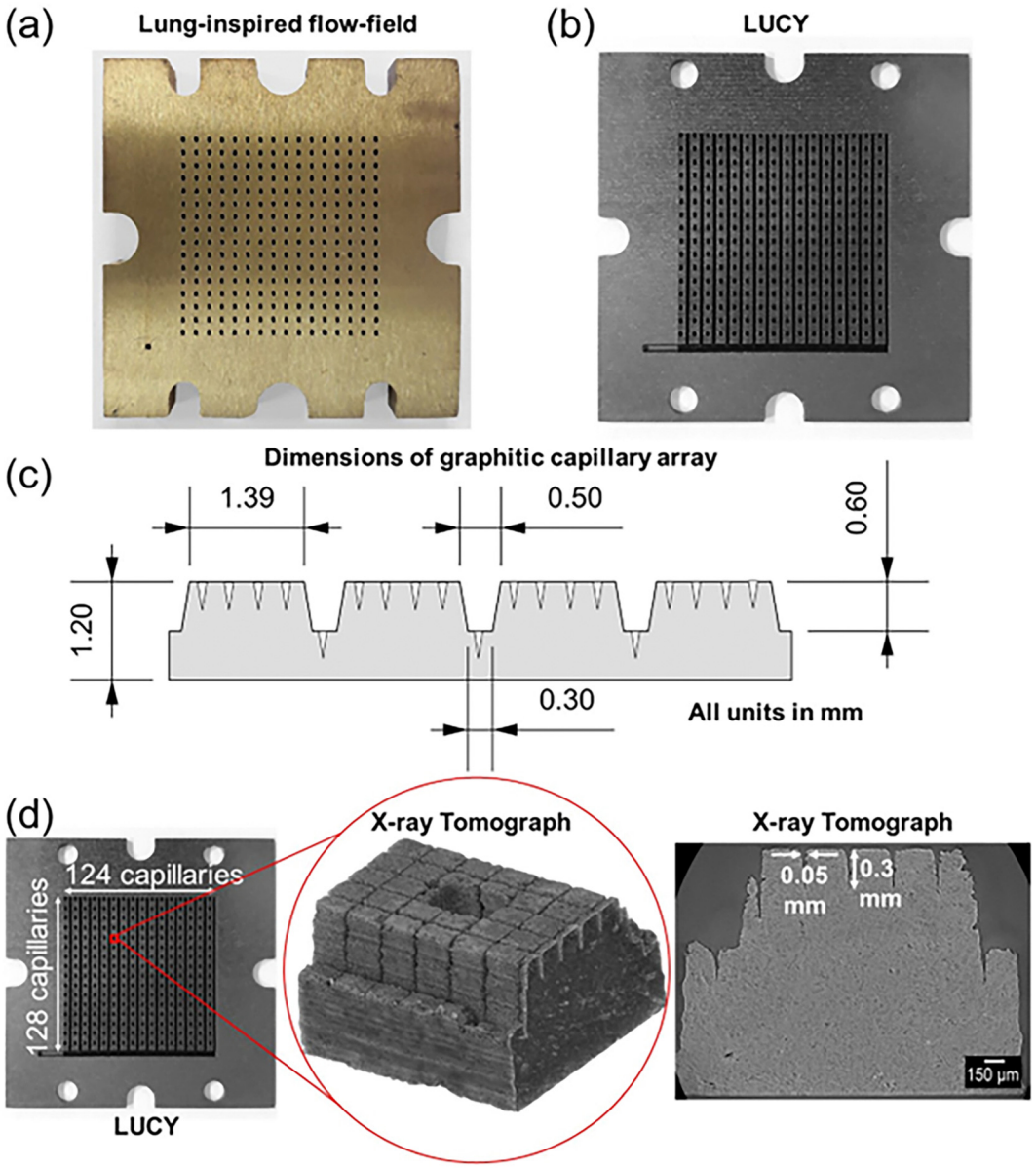

Fig. 2 Engineering of the LUCY flow-field (N = 4 generations and 10 cm^2 surface area) (b). A compact laser micromachining system is used to laser engrave capillaries on a thin graphite plate (c), which is then installed on the surface of the best-performing lung-inspired flow-field (N = 4) (a). X-ray tomographs confirm that LUCY contains 252 laser engraved capillaries, 50 μm wide and 300 μm deep spread uniformly across its surface (d). For the precise fitting of patterned graphite on the flow-field, the capillary regions are separated by a channel 600 μm deep and 300 μm wide.

(*i.e.*, lizard) by a ratio of 9 : 1, we estimated the ratios of gravitational and viscous forces to the capillary forces *via* the Bond number ($B_o = \rho g L^2/\gamma$) and the capillary number ($C_a = \eta u/\gamma$).[37] Here, ρ, γ, and η denote the density (kg m^{-3}), surface tension (N m^{-1}), and dynamic viscosity (Pa s) of water, respectively, while, g is the gravitational acceleration (m s^{-2}), L is the characteristic length of a capillary (m), and u is the characteristic water transport velocity (m s^{-1}) (Table S3 and Section S4.1, ESI†). The characteristic length of a capillary in the integument of the lizard is approximately 150 μm, whereas, in the case of patterned graphite, it is nine-fold larger and equal to 1390 μm. For the natural scale (*i.e.* lizard), the Bond number is approximately $Bo_{1:1} \sim 3 \times 10^{-3}$ and the Capillary number is $Ca_{1:1} \sim 4.3 \times 10^{-5}$, whereas, for the patterned graphite, $Bo_{9:1} \sim 2.7 \times 10^{-3}$ and $Ca_{9:1} \sim 2.9 \times 10^{-5}$, respectively. Since these characteristic numbers remain well below one, capillary forces are dominant over gravitational and viscous forces and control the water transport in this scaled-up structure.[37]

The pressure difference (ΔP) in such capillary can be described by the simplified Young–Laplace equation[37] (derivation of the equation available in Section S4.2, ESI†)

$$\Delta P = \frac{2\gamma \cos(\varphi - \alpha)}{w} \quad (1)$$

where γ is the surface tension of water, φ is the contact angle, α is the tilt angle of capillary side walls, and w is the width of the capillary. The contact angle φ was measured *via* high-speed camera measurements of the water transport within the patterned graphite and is approximately 36°, while the tilt angle α, ~6°, was measured from the tomography images. Thus, the pressure difference in the capillaries on the patterned graphite is >0 and approximately 0.4 kPa, indicating that the water is transported towards the narrowing of the capillary.[37]

X-ray tomographs confirmed that the microchannels are spread uniformly across the graphite plate and their dimensions are 50 μm wide and 300 μm deep (Fig. 2(d)). These were the smallest dimensions that could be engineered, as we were limited by the printing capability of the compact laser micromachining system. Subsequently, this patterned graphite plate with a network of capillaries was aligned and attached to a graphite gasket sheet (Fig. S2, ESI†) with laser cut holes that matched the dimensions of the array of inlets to the best-performing fractal, lung-inspired flow-field (N = 4; Fig. 2(a)). Compression alone is enough to seal these three components (*i.e.*, patterned graphite plate, graphite sheet, and flow-field) together, as in Fig. 3(a). The term "LUCY" (LUng integrated Capillary arraY) will be used throughout the text to describe the lung-inspired flow-field with N = 4 generations and integrated capillary array.

The laser treatment used for the creation of the microchannel structure renders the surface of the capillary channels highly hydrophilic, due to surface oxidation under high temperature and ambient atmosphere. This is evident by Raman measurements, which reveal the presence of the H–O–H bending band of a free water molecule at approximately 1630 cm^{-1} (Fig. S3, ESI†).[45]

The water transport velocity across the engineered capillary channels increases thanks to their hydrophilicity ($\cos\varphi > 0$ or $\varphi < 90°$), as shown by the Washburn equation:[46]

$$\frac{dl}{dt} = \frac{P_o + 2\gamma\cos\varphi\left(r^3 + 4\varepsilon r^2\right)}{8r^2\eta l} \quad (2)$$

where l is the distance travelled along the capillary, t is the time, P_o is the sum of the atmospheric pressure and hydrostatic pressure acting on the liquid, γ is the surface tension, φ is the contact angle, r is the capillary channel radius, η is the viscosity of water (0.001 Pa s), and ε is the coefficient of slip. The contact angle φ (~36°) of water on the patterned graphite surface is smaller than the value (φ ~ 60°) of water on the unstructured capillary material of the lizard,[38] suggesting that the patterned graphite is more hydrophilic than the capillary network of the lizard. Overall, the passive liquid water transport or removal across the surface of the flow-field is similar to the water transport mechanisms of lizards. This is demonstrated by high-speed camera measurements, where the liquid water is instantaneously wicked into the microchannels (~2.3 mm s^{-1} average water transport velocity within LUCY flow-fields, similar to the reported values of ~2.5 and ~3 mm s^{-1} for Arabian and Texan lizards, respectively). (Video S1, ESI†)

The water velocity $\left(\frac{dl}{dt}\right)$ within the engineered graphitic capillary array is calculated by analyzing numerous videos on a frame-to-frame basis. Equation [2] is also integrated numerically to obtain the theoretically predicted water velocity assuming P_o = 0, γ = 72.5 mN m^{-1}, φ = 36°, η = 1 mPa s, and ε = 0.1 by least square fitting.[38] The theoretically predicted velocity is in fairly good agreement with experimental values (Fig. 4(a)), indicating that transport within the patterned graphite plate is indeed dominated by capillary action.[36,43,47] It is also noted that the experimental velocity values of water transport within the capillary array are similar to reported values for the Texan horned lizard and Arabian toad-headed agama (Fig. 4(a)), indicating that the transport mechanism is similarly homogeneous and the animal's mouth, or the exit of the flow-field, serves as a water sink.[47]

Proof-of-concept prototype

These promising characteristics of the lizard-inspired capillary array for fast, passive water transport lead to the next step, namely the demonstration of a proof-of-concept water management strategy for fuel cells. This strategy was first implemented in a commercial, parallel flow-field based PEMFC and evaluated through neutron imaging measurements under galvanostatic operation (Schematic S1, ESI†) with the cell placed in vertical position. The experimental conditions (dry gas in the anode and cathode, ambient fuel cell temperature) for neutron imaging were purposely chosen to reproduce operating conditions limited by flooding. Humidification of the gases and heating of the cell is not recommended to avoid condensation within the cell, which obstructs the through-plane view.[35] Neutron imaging was conducted using counter flow following Toyota's protocol to improve membrane hydration in the absence of gas humidification,[48] where hydrogen is fed from the bottom right of the cell and air is fed from the top left of the cell.

Video S2 (ESI†) shows the behavior of a parallel flow-field based PEMFC at 100% RH. A gradual formation and growth of liquid droplets is observed, which eventually block the gas flow channels and flood the cell. However, once the lizard-inspired capillary array is integrated in this parallel flow-field based PEMFC (Video S3, ESI†), any emerging liquid droplet that comes in contact with the channel wall is immediately wicked towards the outlet (bottom of the channel) and purged shortly after. Tiny water droplets periodically appear at the top and middle of the channel and disappear without growing, demonstrating that water accumulation is eliminated.

The benefits of this anti-flooding water management strategy on fuel cell performance are also readily demonstrated by galvanostatic measurements. The current density and, hence, the associated water production rate within the cell, is gradually increased to examine the behavior of parallel flow-field based PEMFCs with and without integrated capillary array. The flow-field floods after ~20 min using dry inlet gas supply (*i.e.*, all liquid water in the flow-field is produced by the electrochemical reaction) and the fuel cell performance deteriorates. However, once the capillary array is incorporated into these parallel flow-fields, fuel cell performance increases by more

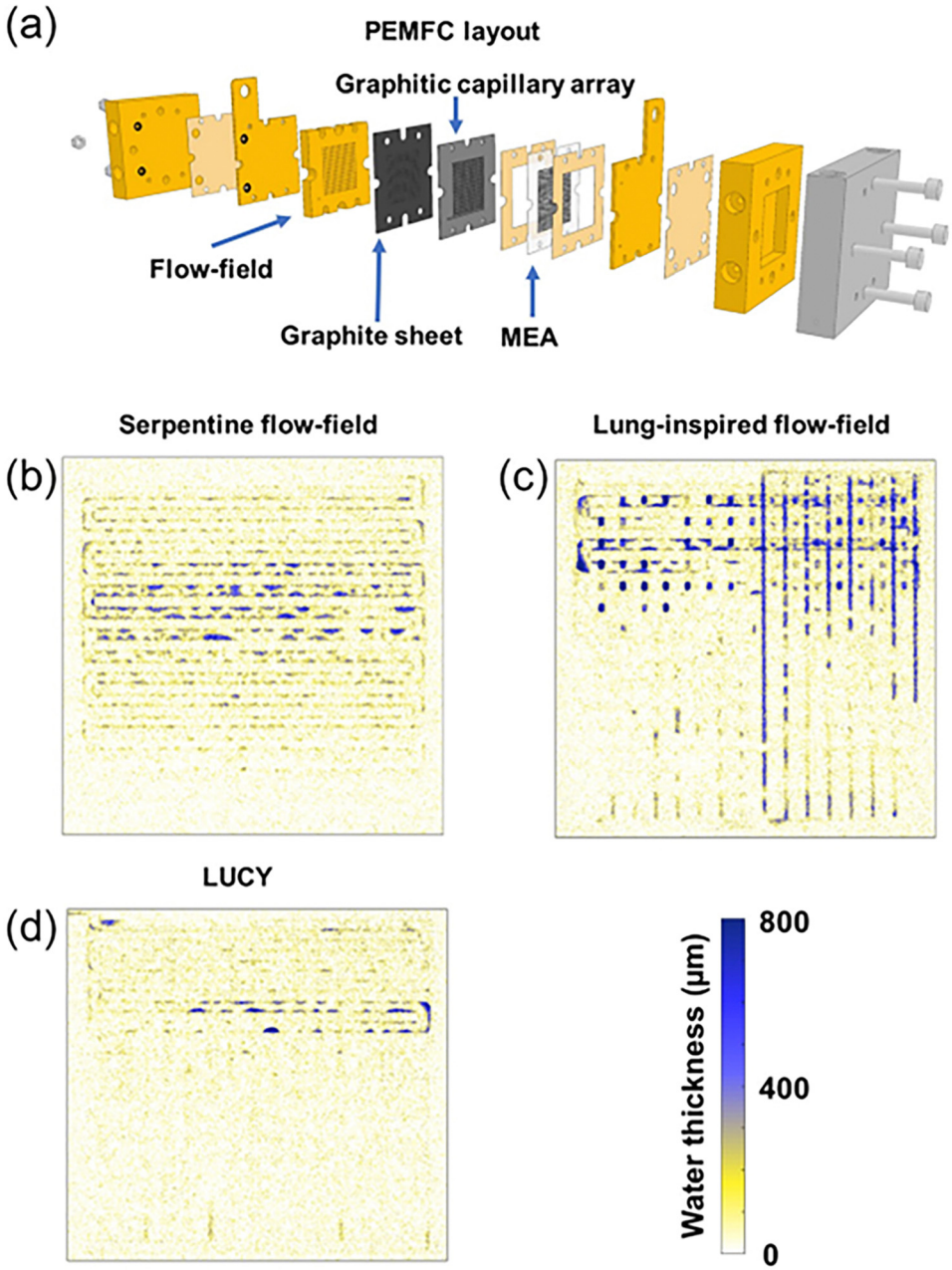

Fig. 3 To evaluate the efficacy of this nature-inspired mechanism, LUCY is assembled into a PEMFC for neutron imaging: (a) Exploded view of the PEMFC assembly: the graphitic capillary array is attached to a graphite sheet with laser cut holes matching the inlet holes of the flow-field in-use and these components are sealed together by compression. Neutron imaging measurements are employed to monitor water distribution across the (b) serpentine, (c) lung-inspired with $N = 4$, and (d) LUCY flow-field based PEMFCs during galvanostatic operation at 0.3 A cm^{-2} (10 cm^2 flow-field area; dry hydrogen and air are used as fuel and oxidant, respectively, with stoichiometric ratios of 1.2 and 3).

than an order-of-magnitude (Fig. 4(b)), showing that this water management strategy prevents the flooding of the cell.

These results suggest that the utilized strategy reduces the dependence of the flow-field on convective gas flow for liquid water removal. The latter helps the performance of serpentine flow-field based PEMFCs, albeit at the cost of a high pressure drop and uneven concentrations. Remarkably, the parallel flow-field based PEMFC with the integrated capillary array performs better than a serpentine flow-field based PEMFC at high current densities (Fig. 4(b)), which suggests enhanced mass transport even without convective gas transport within the electrode.

LUCY flow-field based PEMFC performance measurements

Based on the effectiveness of the lizard-inspired water management strategy, it was integrated in the cathode of our scalable

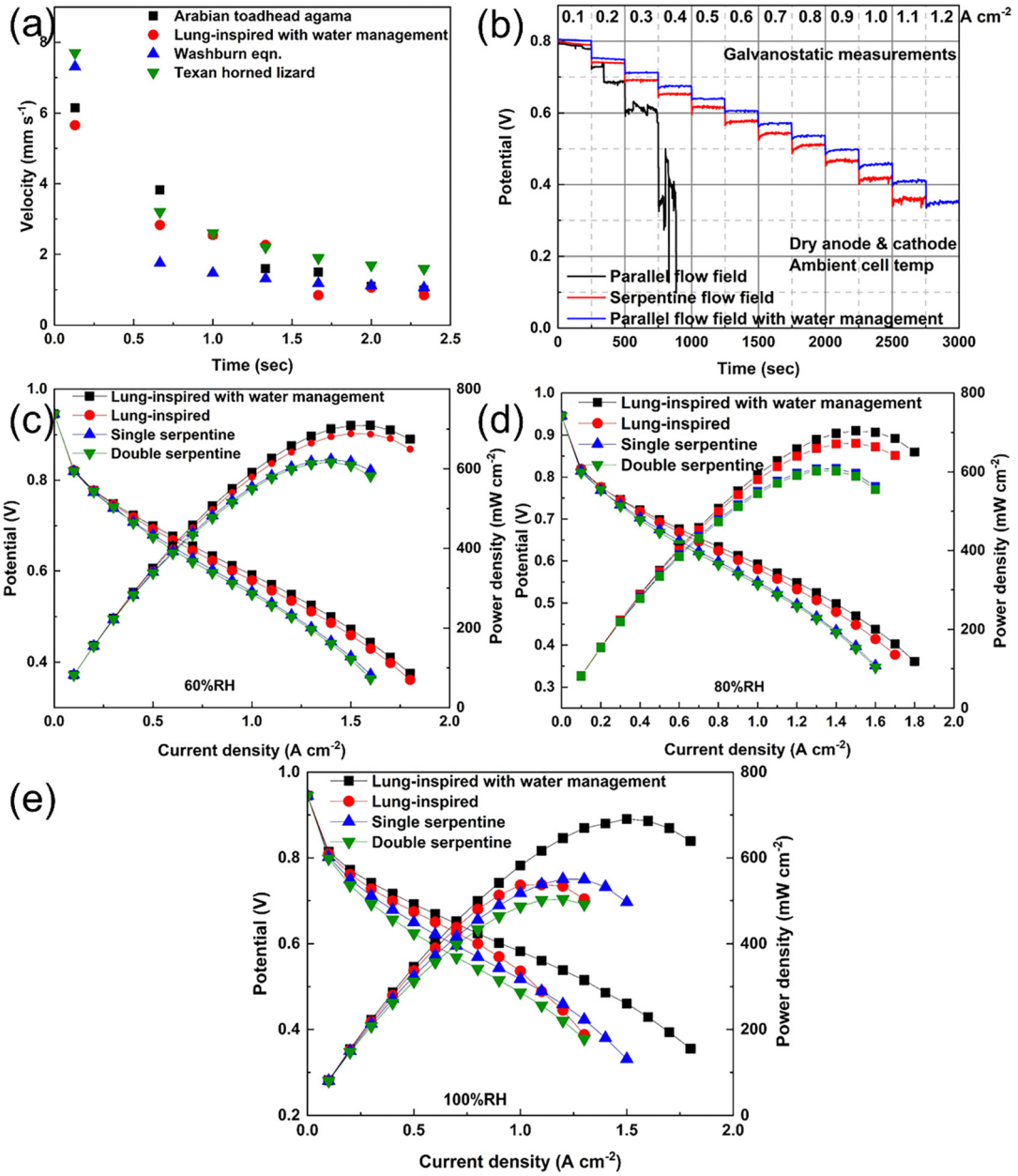

Fig. 4 Following the successful demonstration of the water management ability of a LUCY flow-field *via* neutron imaging measurements, the last step entails the experimental calculation of the water transport velocity within a LUCY flow-field and its installation in a PEMFC: (a) Calculation of the water transport velocity within the lizard-inspired capillary array (10 cm^2 surface area) is performed *via* high-speed camera measurements, and compared with numerical integration of the Washburn equation. These theoretical results reveal that homogeneous, capillary transport of water occurs within the engineered graphitic capillary array, similar to the reported experimental values for lizards living in arid environments. (b) These modeling results guide us to the next step, namely the demonstration of a proof-of-concept, nature-inspired water management strategy for fuel cells: the capillary array is installed on a parallel flow-field based PEMFC and its performance is evaluated under galvanostatic operation. The parallel flow-field based PEMFC with integrated capillary array is flood-free, whereas a parallel flow-field based PEMFC floods after 20 min. The final step is the incorporation of the capillary array into the cathode of our best-performing lung-inspired (N = 4 generations) flow-field based PEMFCs and comparison of its performance at 60% (c), 80% (d), and 100% RH (e) to pristine lung-inspired (N = 4 generations) and serpentine flow-field based PEMFCs, revealing a substantial improvement in PEMFC performance and operating range at 100% RH when implementing a lizard-inspired water management strategy.

lung-inspired flow-field based PEMFCs (N = 4), which had the best electrochemical performance, except at very high relative humidity.[31] We investigated whether the desired features of both nature-inspired solutions could be combined, compared to both an unmodified lung-inspired flow-field and a serpentine flow-field based PEMFC. The polarization measurements were conducted with co-current flow, since humidification of gases is available.[49] The anode side in all flow-field configurations contains a conventional single-serpentine flow-field (10 cm^2 surface area) with channel width, spacing, and

depth of 1 mm, 1 mm, and 0.7 mm, respectively (Section S1.2, ESI†).

In the case of serpentine flow-field based PEMFCs, neutron imaging measurements reveal that water droplets start to gradually proliferate at the corners of the channels of the anode (upper part of Fig. 3(b)) and remain stagnant during the current hold at 0.3 A cm^{-2}, due to the slow gas flow and the absence of a large enough droplet to initiate movement across the channel. However, in the cathode (lower part of Fig. 3(b)), water droplets spread across the channel in the direction of the flow.

On the contrary, the unmodified lung-inspired flow-field's (N = 4) propensity to flooding is evident, due to the slow gas flow. Water droplets merge with neighboring droplets to form slugs, which gradually block the channels and flood the cell, even at low current densities (Fig. 3(c)). Upon the incorporation of the capillary array in these lung-inspired flow-fields (Fig. 3(d)), water accumulation occurs only at the anode, which contains a serpentine flow-field; whereas, at the cathode, the capillaries rapidly remove water from the channels preventing cell flooding. Similar behavior is observed for the serpentine and lung-inspired flow-field based PEMFCs during galvanostatic operation at different current densities.

The fuel cell performance of lung-inspired flow-field (N = 4) and serpentine flow-field based PEMFCs is evaluated at 60%, 80%, and 100% RH. LUCY flow-field based PEMFCs exhibit similar performance at 60% and 80% RH to the pristine lung-inspired flow-field (N = 4) based PEMFC with a ~30% increase in current and power density compared to single- and double-serpentine flow-fields (Fig. 4(c) and (d)). As the relative humidity increases, the performance of the LUCY flow-field based PEMFC gradually increases as well, demonstrating a significant improvement in fuel cell performance and operating range at 100% RH (Fig. 4(e)). Remarkably, the lizard-inspired water management strategy allows flood-free operation at 100% RH for the LUCY flow-field based PEMFC, up to 2 A cm^{-2} and 700 mW cm^{-2} current and power density, respectively; whereas the serpentine and pristine lung-inspired flow-field based PEMFCs have a maximum current and power density of ~1.5 A cm^{-2} and ~500 mW cm^{-2}, respectively, and eventually flood at 100% RH. This exceptional result reveals that the implemented water management strategy effectively utilizes capillary action to remove any produced liquid water even at the highest possible RH, despite the considerably lower pressure drop of the lung-inspired flow-fields (Fig. S4–S6, ESI†). The pressure drop remains constant in the case of LUCY flow-field based PEMFC, irrespective of RH, since there is no channel blockage from produced water, whereas the pressure drop is increasing with higher RH in the case of serpentine and pristine lung-inspired flow-field based PEMFCs, whose channels are gradually flooding. This is in accordance with the measured values of membrane resistance with LUCY flow-field based PEMFC exhibiting the lowest Ohmic resistance (*e.g.*, ~0.42 Ω cm^2 at 100% RH) under all RH tested (Fig. S7–S9, ESI†), suggesting a higher degree of hydration of the polymer membrane and thus higher proton conductivity owing to better water management.[50]

All results are statistically significant. Water transport calculations are based on the analysis of hundreds of images obtained from high-speed camera measurements, while neutron radiographs are obtained from the post-processing of thousands of images taken during neutron imaging. Each point of the polarization curves (Fig. 4) is an average of four measurements (~1% error margin).

Comparison of LUCY flow-field with existing water management strategies

Based on recent, thorough reviews,[21,51] methods for water management in PEMFCs either focus on the modification of the flow-field or the gas diffusion layer (GDL). Our employed method fits in the first category. Another successful design for fuel cell operation at 100% RH consists of so-called water transport plates (WTPs),[52,53] manufactured by United Technologies Corporation (UTC), whereas other flow-field designs reported in the literature, such as radial,[54] Concus-Finn,[55] parallel serpentine-baffle flow-field,[56] or employing parallel channels with different lengths[57] flood at such high humidity conditions. Further recently reported designs of flow-fields, such as an interdigitated, active drainage flow-field[58] and a porous metal (Ni) foam flow-field[59] are flood prone and exhibit significantly lower performance than our flood-free LUCY flow-field based PEMFC (10 cm^2, 2 A cm^{-2} and 700 mW cm^{-2}). The active drainage flow-field (25 cm^2) based PEMFC achieves ~1 A cm^{-2} and ~500 mW cm^{-2} current and power density, respectively, at 100% RH, while the Ni foam flow-field (6 cm^2) based PEMFC demonstrates ~0.8–1 A cm^{-2} current density (power density is not reported). Another approach involves the installation of a coil condenser at the cathode of a 30 kW fuel cell stack, but this results in dehydration of the membrane electrode assembly at working cell temperature ≥45 °C and increased complexity of the fuel cell system.[60]

The performance of the LUCY flow-field based PEMFC surpasses even PEMFCs with installed WTPs in their cathode side at 100% RH.[52,53,61] WTPs are porous bipolar plates with a dual function: the humidification of the reactant at low RH conditions and the drainage of the water from the cell when the GDLs and gas channels are filled with water.[53] The incorporation of WTPs (50 cm^2 surface area) in the cathode of PEMFCs results in an increase of maximum current and power density (~1.5 A cm^{-2} and ~678 mW cm^{-2}, respectively) at 100% RH (H_2/Air as fuel/oxidant) compared to serpentine flow-field based PEMFCs (~1.3 A cm^{-2} and ~600 mW cm^{-2}, respectively).[53,61] Even though these improved performance results at 100% RH are obtained with a 50 cm^2 WTP and 0.4 $mg_{Pt}cm^{-2}$ catalyst loading in the anode and cathode, they are still inferior to the maximum current and power density achieved by our 5 times smaller (10 cm^2) LUCY flow-field based PEMFC with the same catalyst loading and fuel/oxidant ratio, showcasing the superiority of the nature-inspired design in the facile removal of water from the cell at 100% RH.

Additional disadvantages of WTPs include (i) the complexity and total cost of the required fuel cell setup to evaluate its performance, involving custom-made anode and cathode plates

as well as a water chamber, and (ii) the strict requirement for installation of WTPs in both anode and cathode further complicating the setup and increasing the possibility of gas crossover through the water chamber.[52,53,61] If the WTP is employed solely in the cathode, the PEMFC floods and impedes operation at 100% RH.[53] Finally, (iii) there is no detailed information provided about the design principles of WTPs hindering their reproducibility. On the contrary, a LUCY flow-field is only required to be installed at the cathode and a commercial fuel cell station has been used to evaluate its performance, minimizing the complexity and the total cost of the system. Its design principles are detailed in the previous sections, ensuring the reproducibility of the experimental results.

Furthermore, our LUCY flow-field based PEMFC is superior to modified GDLs[62–65] employed for water management at high relative humidity, as these are under development and cannot avoid flooding during operation at 100% RH. A recent example is a Janus GDL[66] consisting of hydrophobic and hydrophilic layers. Its antiflooding ability has only been reported in a half-cell, not in an actual fuel cell, thus, it cannot be compared to the performance of our LUCY flow-field based PEMFC. Another example[67] is a GDL based on nanoporous gold film; information about the actual size of the PEMFC is missing while its performance is evaluated employing H_2/O_2 as oxidant (instead of H_2/Air in our case), yet still resulting in lower performance at 100% RH with our LUCY flow-field based PEMFC and stability challenges.

Conclusions

A nature-inspired methodology is employed to solve an important issue in PEMFCs, namely their flooding at high relative humidity. The water drinking mechanism of lizards residing in arid environments, based on capillary action, constitutes the source of inspiration.

The water management strategy adopted is different to that reported previously,[49] as it is based solely on capillary pressure to remove the water from the fuel cell, instead of the pressure difference between the gas and liquid water channel.[49] Disregarding the geometric characteristics of the capillary network within the integument of the lizards would not lead to a successful flow-field design, since its ability for water removal would still depend on pressure drop, as is the case for conventional flow-fields. This is demonstrated in recent reports mimicking the water drinking mechanism of certain desert beetles, which bears similarities to the one of lizards living in arid environments, to improve the water management within a PEMFC.[50,68] Only the hydrophilic surface of the integument of the desert beetle constitutes the source of inspiration and a hydrophilic coating is applied within the channels of a conventional flow-field; the network of micro-sized grooves that transports the water from its integument to its mouth is not considered.[50,68] As a result, water removal from such bio-imitating flow-fields still relies on pressure drop (gas transport) with questionable stability, reproducibility, and scalability, as, at larger scales, pressure drop within the flow-field significantly increases, thus enhancing parasitic energy losses.[31]

In our work, a thin graphite plate with laser-engraved microchannel structure is engineered *via* a compact laser micromachining system and installed in a commercial flow-field (serpentine and parallel) and our best performing lung-inspired flow-field ($N = 4$) based PEMFCs. As a proof-of-concept, the water management strategy is first implemented on a parallel flow-field, exhibiting larger than one order-of-magnitude improvement in performance at 100% RH compared to a parallel flow-field based PEMFC. The capillary array is then installed in a lung-inspired ($N = 4$) flow-field based PEMFC, demonstrating flood-free operation and a substantial increase in current and power density at 100% RH compared to serpentine and our pristine lung-inspired ($N = 4$) flow-field based PEMFCs, which rapidly flood under these conditions.

Moreover, the addition of this fixture to our lung-inspired flow-field based PEMFC does not alter the pressure drop within the flow-field, which retains the lowest value (less than $\sim$0.07 bar for a 10 cm^2 surface area) among all the flow-fields tested ($\sim$0.12 bar for a 10 cm^2 surface area of serpentine flow-field). Such a low pressure drop favors the use of a large-scale lung-inspired flow-field, as it minimizes parasitic losses.

The design of the microchannel structure of the capillary array for effective water management within the flow-field can be improved by leveraging another extraordinary trait of these lizards, namely the directionality of the flow, since water is preferentially transported from any location on their skin towards their snout.[37,38] This directional liquid transport is achieved by a periodic pattern of asymmetric capillaries, where the width of each capillary channel gradually narrows towards their snout.[37] Such a trait could allow for an additional degree of control over the transportation of water across the surface of the flow-field and will be the subject of a future study.

The water management ability of the proposed nature-inspired flow field can also be further improved *via* the implementation of state-of-the-art GDLs, such as the Freudenberg GDL.[69] Its low thermal conductivity leads to significant temperature gradients between the catalyst layer and the channels of the flow field, enhancing water removal at high current densities.[69]

Finally, the low cost and facile engineering of the proposed water management strategy favors mass production for PEMFCs, even though its scalability also depends on the width of each capillary. For larger PEMFCs, this value might not be small enough to prevent gas breakthrough in the water transport network, since gas pressure significantly increases during scale-up. An advanced compact laser micromachining system (*e.g.*, femtosecond laser) is required to create capillaries with smaller diameters. In terms of the scalability of lung-inspired flow-fields manufactured *via* 3D laser sintering,[31] their high cost ($\sim$£800 per flow-field), weight ($\sim$0.5 kg per flow-field) and manufacturing time ($\sim$1 week per flow-field) can be significantly decreased ($\sim$£50, 30 g weight and 2 days of preparation per flow-field) using printed circuit board as the construction material, instead of stainless steel.[70,71]

Nomenclature

BEV	Battery powered electric vehicle
Bo	Bond number
Ca	Capillary number
GDLs	Gas diffusion layers
FCV	Fuel cell powered electric vehicle
LUCY	LUng integrated Capillary arraY
MEA	Membrane electrode assembly
NICE	Nature-inspired chemical engineering
PEMFC	Proton exchange membrane fuel cell
RH	Relative humidity
RHE	Reversible hydrogen electrode
WTPs	Water transport plates

Author contributions

J. I. S. Cho and M.-O. Coppens conceived the idea. P. Trogadas, J. I. S. Cho, and D. J. L. Brett conceived the experiments. J. I. S. Cho, P. Trogadas, L. Rasha, D. J. L. Brett, M.-O. Coppens conducted the electrochemical measurements and/or contributed to data analysis. X. Lu and P. R. Shearing conducted X-ray tomography measurements and data analysis. J. I. S. Cho, N. Kardjilov, H. Markötter, I. Manke conducted Neutron imaging measurements and/or contributed to data analysis. P. Trogadas and J. I. S. Cho conducted Raman and high-speed camera measurements and contributed to data analysis. P. Trogadas wrote the manuscript, and all authors were involved in revising the manuscript.

Conflicts of interest

There are no conflicts of interest to declare.

Acknowledgements

The authors gratefully acknowledge funding from EPSRC through an EPSRC "Frontier Engineering" Grant (EP/K038656/1), an EPSRC "Frontier Engineering: Progression" Grant (EP/S03305X/1), and Studentship Grants (EP/N509577/1, EP/T517793/1) supporting nature-inspired electrochemical research in the Centre for Nature Inspired Engineering (CNIE) and fuel cell research (EP/L015277/1, EP/P009050/1, EP/M014371/1, EP/M009394/1, EP/M023508/1, EP/L015749/1, EP/N022971/1) in the Electrochemical Innovation Lab (EIL). Helmholtz-Zentrum Berlin is gratefully acknowledged for support in neutron-imaging measurements of PEMFCs.

References

1 E. Zeyen, M. Victoria and T. Brown, *Nat. Commun.*, 2023, **14**, 3743.
2 G. Squadrito, G. Maggio and A. Nicita, *Renewable Energy*, 2023, **216**, 119041.
3 S. van Renssen, *Nature Climate Change*, 2020, **10**, 799–801.
4 A. Rinaldi, A. Syla, M. K. Patel and D. Parra, *Cleaner Prod. Lett.*, 2023, **5**, 100044.
5 IEA, **https://www.iea.org/reports/global-ev-outlook-2023**, 2023.
6 A. Rudola, R. Sayers, C. J. Wright and J. Barker, *Nat. Energy*, 2023, **8**, 215–218.
7 Y. Li and S. Kimura, *Energy Policy*, 2021, **148**, 111980.
8 K. Jiao, J. Xuan, Q. Du, Z. Bao, B. Xie, B. Wang, Y. Zhao, L. Fan, H. Wang, Z. Hou, S. Huo, N. P. Brandon, Y. Yin and M. D. Guiver, *Nature*, 2021, **595**, 361–369.
9 G. Trencher and J. Wesseling, *Transp. Res. Part D: Transp. Environ.*, 2022, **112**, 103458.
10 D. A. Cullen, K. C. Neyerlin, R. K. Ahluwalia, R. Mukundan, K. L. More, R. L. Borup, A. Z. Weber, D. J. Myers and A. Kusoglu, *Nat. Energy*, 2021, **6**, 462–474.
11 IEA, **https://ieahev.org/wp-content/uploads/2023/05/Task-35-_final-report-2022-0627.pdf**, 2022.
12 S. Biswas, K. Moreno Sader and W. H. Green, *Energy Fuels*, 2023, **37**, 17003–17012.
13 U.S.DOE, **https://www.energy.gov/eere/fuelcells/doe-technical-targets-fuel-cell-systems-stationary-combined-heat-and-power** and **https://www.energy.gov/eere/fuelcells/doe-technical-targets-fuel-cell-systems-and-stacks-transportation-applications**, 2020.
14 R. Borup, J. Meyers, B. Pivovar, Y. S. Kim, R. Mukundan, N. Garland, D. Myers, M. Wilson, F. Garzon, D. Wood, P. Zelenay, K. More, K. Stroh, T. Zawodzinski, J. Boncella, J. E. McGrath, M. Inaba, K. Miyatake, M. Hori, K. Ota, Z. Ogumi, S. Miyata, A. Nishikata, Z. Siroma, Y. Uchimoto, K. Yasuda, K.-I. Kimijima and N. Iwashita, *Chem. Rev.*, 2007, **107**, 3904–3951.
15 N. Macauley, D. D. Papadias, J. Fairweather, D. Spernjak, D. Langlois, R. Ahluwalia, K. L. More, R. Mukundan and R. L. Borup, *J. Electrochem. Soc.*, 2018, **165**, F3148–F3160.
16 G. Shen, J. Liu, H. B. Wu, P. Xu, F. Liu, C. Tongsh, K. Jiao, J. Li, M. Liu, M. Cai, J. P. Lemmon, G. Soloveichik, H. Li, J. Zhu and Y. Lu, *Nat. Commun.*, 2020, **11**, 1191.
17 P. Deevanhxay, T. Sasabe, S. Tsushima and S. Hirai, *Electrochem. Commun.*, 2012, **22**, 33–36.
18 Y. Sun, S. Polani, F. Luo, S. Ott, P. Strasser and F. Dionigi, *Nat. Commun.*, 2021, **12**, 5984.
19 J. Kwon and K. Eom, *J. Phys. Chem. C*, 2021, **125**, 10824–10834.
20 M. Vinothkannan, R. Hariprasad, S. Ramakrishnan, A. R. Kim and D. J. Yoo, *ACS Sustainable Chem. Eng.*, 2019, **7**, 12847–12857.
21 X. R. Wang, Y. Ma, J. Gao, T. Li, G. Z. Jiang and Z. Y. Sun, *Int. J. Hydrogen Energy*, 2021, **46**, 12206–12229.
22 W. Yoshimune, S. Kato, S. Yamaguchi, Y. Akimoto, A. Koiwai and H. Nakamura, *ACS Sustainable Chem. Eng.*, 2021, **9**, 7922–7929.
23 W. E. Mustain, M. Chatenet, M. Page and Y. S. Kim, *Energy Environ. Sci.*, 2020, **13**, 2805–2838.
24 Y. Yang, P. Li, X. Zheng, W. Sun, S. X. Dou, T. Ma and H. Pan, *Chem. Soc. Rev.*, 2022, **51**, 9620–9693.
25 I. Vincent, E.-C. Lee and H.-M. Kim, *RSC Adv.*, 2020, **10**, 16844–16860.
26 A. Reyes, R. P. Jansonius, B. A. W. Mowbray, Y. Cao, D. G. Wheeler, J. Chau, D. J. Dvorak and C. P. Berlinguette, *ACS Energy Lett.*, 2020, **5**, 1612–1618.
27 D. G. Wheeler, B. A. W. Mowbray, A. Reyes, F. Habibzadeh, J. He and C. P. Berlinguette, *Energy Environ. Sci.*, 2020, **13**, 5126–5134.

28 R. Haider, Y. Wen, Z.-F. Ma, D. P. Wilkinson, L. Zhang, X. Yuan, S. Song and J. Zhang, *Chem. Soc. Rev.*, 2021, **50**, 1138–1187.
29 M.-O. Coppens, *Annu. Rev. Chem. Biomol. Eng.*, 2021, **12**, 187–215.
30 P. Trogadas and M.-O. Coppens, *Chem. Soc. Rev.*, 2020, **49**, 3107–3141.
31 P. Trogadas, J. I. S. Cho, T. P. Neville, J. Marquis, B. Wu, D. J. L. Brett and M. O. Coppens, *Energy Environ. Sci.*, 2018, **11**, 136–143.
32 J. I. S. Cho, J. Marquis, P. Trogadas, T. P. Neville, D. J. L. Brett and M. O. Coppens, *Chem. Eng. Sci.*, 2020, **215**, 115375.
33 S. Gheorghiu, S. Kjelstrup, P. Pfeifer and M.-O. Coppens, In: Fractals in Biology and Medicine, ed. G.A. Losa, D. Merlini, T.G. Nonnenmacher and E.R. Weibel, Birkhäuser, Basel, 2005, vol. IV, 31–42.
34 B. Mauroy, M. Filoche, E. R. Weibel and B. Sapoval, *Nature*, 2004, **427**, 633–636.
35 J. I. S. Cho, T. P. Neville, P. Trogadas, Q. Meyer, Y. Wu, R. Ziesche, P. Boillat, M. Cochet, V. Manzi-Orezzoli, P. Shearing, D. J. L. Brett and M. O. Coppens, *Energy*, 2019, **170**, 14–21.
36 P. J. Bentley and W. F. C. Blumer, *Nature*, 1962, **194**, 699–700.
37 P. Comanns, G. Buchberger, A. Buchsbaum, R. Baumgartner, A. Kogler, S. Bauer and W. Baumgartner, *J. R. Soc., Interface*, 2015, **12**, 20150415.
38 P. Comanns, C. Effertz, F. Hischen, K. Staudt, W. Böhme and W. Baumgartner, *Beilstein J. Nanotechnol.*, 2011, **2**, 204–214.
39 P. Comanns, F. J. Esser, P. H. Kappel, W. Baumgartner, J. Shaw and P. C. Withers, *R. Soc. Open Sci.*, 2017, **4**, 170591.
40 P. Comanns, P. C. Withers, F. J. Esser and W. Baumgartner, *J. Exp. Biol.*, 2016, **219**, 3473.
41 W. C. Sherbrooke, *J. Herpetol.*, 1993, **27**, 270–275.
42 W. C. Sherbrooke, A. J. Scardino, R. de Nys and L. Schwarzkopf, *Zoomorphology*, 2007, **126**, 89–102.
43 C. Gans, R. Merlin and W. Blumer, *Amphibia-reptilia*, 1982, **3**, 57–64.
44 W. Sherbrooke, *Amphib. Reptiles*, 2004, **25**, 29–39.
45 C.-C. Yu, K.-Y. Chiang, M. Okuno, T. Seki, T. Ohto, X. Yu, V. Korepanov, H.-O. Hamaguchi, M. Bonn, J. Hunger and Y. Nagata, *Nat. Commun.*, 2020, **11**, 5977.
46 E. W. Washburn, *Phys. Rev.*, 1921, **17**, 273–283.
47 P. Withers, *J. Herpetol.*, 1993, **27**, 265–270.
48 T. Yoshida and K. Kojima, *Electrochem. Soc. Interface*, 2015, **24**, 45.
49 J. I. S. Cho, T. P. Neville, P. Trogadas, J. Bailey, P. Shearing, D. J. L. Brett and M. O. Coppens, *Int. J. Hydrogen Energy*, 2018, **43**, 21949–21958.
50 T. Zhao, K. Jiang, W. Fan, D. Lu, D. Zheng, H. Cui, L. Yang, G. Lu and Z. Liu, *Chem. Eng. J.*, 2023, **466**, 143288.
51 H. Pourrahmani, A. Yavarinasab, M. Siavashi, M. Matian and J. Van Herle, *Energy Rev.*, 2022, **1**, 100002.
52 X. Guo, Y. Zeng, Z. Wang, Z. Shao and B. Yi, *J. Power Sources*, 2016, **302**, 84–91.
53 Z. Wang, Y. Zeng, S. Sun, Z. Shao and B. Yi, *Int. J. Hydrogen Energy*, 2017, **42**, 21922–21929.
54 B. R. Friess and M. Hoorfar, *Int. J. Hydrogen Energy*, 2012, **37**, 7719–7729.
55 S. H. Han, N. H. Choi and Y. D. Choi, *Renewable Energy*, 2012, **44**, 88–98.
56 P. Martins Belchor, M. M. Camargo Forte and D. E. Ortiz Suman Carpenter, *Int. J. Hydrogen Energy*, 2012, **37**, 11904–11911.
57 J. Bachman, M. Charvet, A. Santamaria, H.-Y. Tang, J. W. Park and R. Walker, *Int. J. Hydrogen Energy*, 2012, **37**, 17172–17179.
58 Y. Wang, L. Wang, X. Ji, Y. Zhou and M. Wu, *ACS Omega*, 2021, **6**, 21892–21899.
59 L. Chen, Z. Wang, C. Sun, H. Zhu, Y. Xia, G. Hu and B. Fang, *Micromachines*, 2023, **14**, 1224.
60 B. Xiao, Z. Huang, Z. Tu and S. H. Chan, *Int. J. Hydrogen Energy*, 2023, **48**, 10671–10683.
61 Z. Wang, L. Qu, Y. Zeng, X. Guo, Z. Shao and B. Yi, *RSC Adv.*, 2018, **8**, 1503–1510.
62 I. Bae, B. Kim, D.-Y. Kim, H. Kim and K.-H. Oh, *Renewable Energy*, 2020, **146**, 960–967.
63 R. Lin, X. Diao, T. Ma, S. Tang, L. Chen and D. Liu, *Appl. Energy*, 2019, **254**, 113714.
64 D. Spernjak, R. Mukundan, R. L. Borup, L. G. Connolly, B. I. Zackin, V. De Andrade, M. Wojcik, D. Y. Parkinson, D. L. Jacobson, D. S. Hussey, K. L. More, T. Chan, A. Z. Weber and I. V. Zenyuk, *ACS Appl. Energy Mater.*, 2018, **1**, 6006–6017.
65 D.-H. Lee, G.-T. Yun, G. Doo, S. Yuk, H. Guim, Y. Kim, W.-B. Jung, H.-T. Jung and H.-T. Kim, *Nano Lett.*, 2022, **22**, 1174–1182.
66 Q. Wen, S. Pan, Y. Li, C. Bai, M. Shen, H. Jin, F. Ning, X. Fu and X. Zhou, *ACS Energy Lett.*, 2022, **7**, 3900–3909.
67 J. Jia, X. Liu, F. Liu, H. Yin and Y. Ding, *Int. J. Hydrogen Energy*, 2022, **47**, 21261–21272.
68 Z. Liu, T. Zhao, W. Fan, X. Men, K. Jiang and G. Lu, *ACS Appl. Nano Mater.*, 2022, **5**, 2280–2292.
69 H. Xu, M. Bührer, F. Marone, T. J. Schmidt, F. N. Büchi and J. Eller, *J. Electrochem. Soc.*, 2021, **168**, 074505.
70 V. S. Bethapudi, J. Hack, P. Trogadas, J. I. S. Cho, L. Rasha, G. Hinds, P. R. Shearing, D. J. L. Brett and M. O. Coppens, *Energy Convers. Manage.*, 2019, **202**, 112198.
71 V. S. Bethapudi, J. Hack, P. Trogadas, G. Hinds, P. R. Shearing, D. J. L. Brett and M. O. Coppens, *Energy Convers. Manage.*, 2020, **220**, 113083.